Nanoscale

PAPER

View Article Online
View Journal | View Issue

Check for updates

Cite this: *Nanoscale*, 2024, **16**, 14339

Novel nitrogen-doped carbon-coated $SnSe_2$ based on a post-synthetically modified MOF as a high-performance anode material for LIBs and SIBs†

Zhiyuan Chen,[a] Zhe Zhang,[a] Longzhen Wang,[a] Yifei Li,[a] Yiting Wang,[a] Yichuan Rui,[a] Ailing Song,*[b] Min Li,[c] Yinyu Xiang,[d] Kaibin Chu,[e] Lei Jiang,*[f] Bohejin Tang,*[a] Ning Han,[g] Guoxiu Wang[h] and Hao Tian*[h]

$SnSe_2$ with high theoretical capacity has been identified as an emerging anode candidate for lithium-ion batteries (LIBs) and sodium-ion batteries (SIBs). However, the rate performance and cycling performance of this material in practical applications are still limited by unavoidable volume expansion and low conductivity. In this work, we designed and synthesized nitrogen-doped carbon-coated $SnSe_2$/C–N composites using 2-aminoterephthalic acid ($C_8H_7NO_4$) as a nitrogen-containing compound for modification by hydrothermal and vacuum calcination methods to achieve efficient utilization of active sites and optimization of the electronic structure. The carbon skeleton inherited from the Sn-MOF precursor can effectively improve the electronic conduction properties of $SnSe_2$. N-doping in the Sn-MOF can increase the positive and negative electrostatic potential energy regions on the molecular surface to further improve the electrical conductivity, and effectively reduce the binding energy with Li^+/Na^+ which was determined by Density Functional Theory (DFT) methods. In addition, the N-doped carbon skeleton also introduces a larger space for Li^+/Na^+ intercalation and enhances the mechanical properties. In particular, the post-synthetically modified MOF-derived $SnSe_2$/C–N materials exhibit excellent cyclability, with a reversible capacity of 695 mA h g^{-1} for LIBs and 259 mA h g^{-1} for SIBs after 100 cycles at 100 mA g^{-1}.

Received 12th June 2024,
Accepted 10th July 2024

DOI: 10.1039/d4nr02418d

rsc.li/nanoscale

Published on 11 July 2024. Downloaded on 4/29/2026 2:52:14 AM.

Introduction

The emergence of the energy crisis and the escalating climate change situation have led to the consideration of large-scale application of secondary energy resources, such as solar and wind energy.[1] This is seen as a feasible solution to reduce the overuse of petroleum fuels and alleviate ecological pollution.[2–6] Therefore, there is an urgent need to develop and explore a green and recyclable energy storage and conversion system.[7] As an energy storage device that meets the above requirements, lithium-ion batteries (LIBs) are widely used in various academic and industrial fields such as mobile power, new energy vehicles, and aerospace due to their high quality/volumetric energy density, and no memory effect.[8–17] Although LIBs have developed into a mature technology, the fact that there are limited Li resources has prompted researchers not to focus solely on Li^+, thus stimulating research on sodium-ion batteries (SIBs), which are based on the more abundant Na metal element.[18] Moreover, the intercalation reaction chemistry of LIBs and SIBs exhibits striking similarities, thereby making SIBs function in a manner akin to LIBs.[19,20] Due to their excellent electrochemical and safety properties, LIBs and SIBs have been receiving continuing attention from researchers around the world.[21,22]

The composition and structure of the anode material have a decisive influence on the electrochemical performance of

[a]College of Chemistry and Chemical Engineering, Shanghai University of Engineering Science, Shanghai 201620, People's Republic of China. E-mail: tangbohejin@sues.edu.cn
[b]College of Environmental and Chemical Engineering, Yanshan University, Qinhuangdao, China. E-mail: ailing.song@ysu.edu.cn
[c]Department of Industrial Chemistry, University of Bologna, Viale Risorgimento 4, 40136 Bologna, Italy
[d]School of Chemistry, Chemical Engineering and Life Sciences, Wuhan University of Technology, Wuhan 430070, China
[e]School of Materials Science and Engineering, Linyi University, Linyi, 276000, P. R. China
[f]Department of Chemical Engineering, KU Leuven, Celestijnenlaan 200F, B-3001 Heverlee, Belgium. E-mail: lei.jiang@kuleuven.be
[g]Department of Materials Engineering, KU Leuven, Leuven, 3001, Belgium
[h]Centre for Clean Energy Technology, School of Mathematical and Physical Sciences, Faculty of Science, University of Technology Sydney, Broadway, Sydney, NSW, 2007, Australia. E-mail: Hao.tian@uts.edu.au

†Electronic supplementary information (ESI) available: Fig. S1–S4. See DOI: https://doi.org/10.1039/d4nr02418d

Published on 11 July 2024. Downloaded on 4/29/2026 2:52:14 AM.

LIBs and SIBs.[23,24] Transition metal compounds have been widely investigated because they have sufficient reactive active sites and short Li^+ and Na^+ diffusion paths, which are conducive to the electrochemical performance of anode materials.[25–28] Metal selenides (MSe_x) with a layered structure offer superior performance over metal chalcogenides in many aspects in typical conversion anode materials for secondary batteries.[29,30] Compared with metal oxides, the weaker M–Se bond compared to the M–O bond facilitates the smooth progress of the conversion reaction, and the alkali metal ions may migrate rapidly with lower diffusion energy barriers supported by the larger layer spacing and weaker van der Waals force interactions.[31] In addition, compared with metal sulfides, selenium atoms have larger atomic radii and stronger metallicity than sulfur atoms, resulting in metal selenides with larger layer spacing and higher conductivity.[32]

As the representatives of reactive MSe_x, SnSe/$SnSe_2$ materials have high theoretical activity through successive intercalation and transformation reactions producing reactive metals that will further form alloys with Li and Na.[33] For example, with 1 mol e^- involved in the reaction calculations, the theoretical sodium storage capacities of SnSe and $SnSe_2$ in SIB anodes are 780 mA h g^{-1} and 756 mA h g^{-1}, respectively, which are very impressive for the field of stored Na^+ research.[34,35] These compounds have a large layer spacing due to their typical lamellar structure, thus facilitating easy intercalation of bulkier active metal ions.[36] However, tin selenide active materials undergo unavoidable volume expansion and particle agglomeration during the alloying/de-alloying process, resulting in a significant decrease in reversible capacity.[37,38] However, the inherently poor electrical conductivity of SnSe/$SnSe_2$ and the high cost of industrialized synthesis methods severely hinder the utilization of their excellent theoretical capacity.[39] To overcome the above shortcomings of tin selenides, studies have shown that carbon coatings are effective in reducing the occurrence of side reactions, enhancing the electrical conductivity of the material, and mitigating drastic volume changes in the material due to stress residues, maintaining the stability of the main structure.[40–44] Combining carbon skeletons with transition metal compounds to make composites can capitalize on the powerful synergistic effects brought about by heterogeneous structural engineering, mitigating the volumetric expansion of the materials that occurs during cyclic intercalation while significantly improving electrical conductivity.[45–49] What's more, by incorporating N atoms into the carbon skeleton, the electronic property modulation effect of N atoms can significantly change the charge and spin densities of carbon atoms, and the carbon material becomes non-electronic and neutral, which is favorable for the oxygen reduction reaction on carbon.[50–52] That is to say, compounding with conductive carbon skeletons based on nitrogen doping may be one of the effective ways to overcome the disadvantages of existing SnSe/$SnSe_2$ anode materials.[53–56]

Metal–organic frameworks (MOFs) are organic–inorganic hybrid crystalline materials with intramolecular pores that result from the self-assembly of metal ions or clusters in organic ligands and coordination bonds.[57–59] They have attracted much attention from researchers because of their tuneable porosity, abundant active centres and controllable morphology.[60–62] It has been reported that using MOFs as sacrificial templates can produce a specific porous structural morphology, and most of the functional materials obtained inherit the morphological structure of the MOF precursors.[63,64] The use of organic ligands containing N for the pretreatment of MOF precursors and the synergistic doping effect of trace heteroatoms on the carbon skeleton can also effectively enhance the activity and stability of the carbon skeleton.[65–68]

In this work, we synthesized an Sn-MOF using a low-temperature hydrothermal method, and then used 2-aminoterephthalic acid ($C_8H_7NO_4$) to replace the solvent sites in the MOF clusters, and further heat-treated it with selenium under vacuum to synthesize nitrogen-loaded carbon-capped $SnSe_2$/C–N. According to the previous reports of our group, the Sn-MOF can effectively replace the solvent sites in MOF clusters by injecting an organic nitrogen source after heat treatment under vacuum, and the organic ligand ($C_8H_7NO_4$) is converted to an impurity-free N-loaded carbon source during the subsequent selenization process.[65] The N-loaded carbon skeleton derived from the Sn-MOF precursor can limit the volume expansion of the material during the cycling process. The modification of the Sn-MOF, employing organic ligands to replace solvent sites in MOF clusters, is not only carried out to enhance the mechanical properties of the carbon framework, but also to bring a wider layer spacing and more chemically reactive sites to the carbon skeleton and further improve the conductivity of this material.[69,70] In addition, N atoms are incorporated into the carbon skeleton as dopants to further enhance the redox activity based on the synergistic effect.[71] In particular, the post-synthetically modified MOF-derived $SnSe_2$/C–N material exhibits excellent cyclability with a reversible capacity of 695 mA h g^{-1} for LIBs and a reversible capacity of 259 mA h g^{-1} for SIBs after 100 cycles at a current density of 100 mA g^{-1}, respectively.

Experimental section

Synthesis of the Sn-MOF

The raw materials used in the experiments were commercially available, analytically pure chemicals without pretreatment. The Sn-MOF was synthesised using a simple one-step low-temperature hydrothermal method as reported in previous work. First, 1.073 g of $SnSO_4$ was dissolved in a beaker with 25 ml of deionized (DI) water and sonicated for 10 minutes to form a homogeneous $SnSO_4$ solution. Subsequently, 1.007 g of lithium hydroxide (LiOH) and 1.993 g of terephthalic acid ($C_8H_6O_4$) were ultrasonically dissolved in 100 ml of a mixture of *N*,*N*-dimethylformamide (DMF) and DI water (V_{DMF}/V_{water}, 1 : 1) in the same manner. The $SnSO_4$ solution was then slowly added dropwise to the mixed LiOH + $C_8H_6O_4$ solution and magnetically stirred at 50 °C for 2 h. Finally, the precipitate

 This journal is © The Royal Society of Chemistry 2024

Published on 11 July 2024. Downloaded on 4/29/2026 2:52:14 AM.

was washed by centrifugation with DMF and deionised water in turn to obtain a white product, which was dried under vacuum at 70 °C for one day to obtain the Sn-MOF.

Synthesis of Sn/C and $SnSe_2$/C

The Sn-MOF was then placed in a porcelain boat and gradually heated to 450 °C at a rate of 4 °C per minute under an Ar/H_2 (10%) atmosphere and held for 6 hours to obtain Sn/C. The selenization process may lead to impurity in the final products and insufficient reaction when a protective atmosphere of inert gas is used. Based on the successful preparation of V_3S_4/CNF by vacuum vulcanization,[72] and our previous work,[65] the selenization process can be carried out under vacuum conditions, achieving complete reaction and pure products. For our work, a mixture of Sn/C and selenium powder (mass ratio, $M_{Sn/C}/M_{Se}$, 1 : 3) was placed in a vacuum quartz tube, and then gradually heated to 600 °C and kept in a muffle furnace for 6 h. The product obtained by centrifugation was washed 3 times with ethanol and carbon disulfide to remove unreacted selenium powder, and dried under vacuum at 80 °C for 24 h to obtain $SnSe_2$/C.

Synthesis of $SnSe_2$/C–N

Prior to the formal synthesis of $SnSe_2$/C–N, the Sn-MOF sacrificial template precursor required additional nitrogen doping treatment. The Sn-MOF was placed in a glass flask and dried under vacuum at 180 °C for 4 h to remove water molecules from the cluster cores. Then 2-aminoterephthalic acid (mass ratio, $M_{Sn\text{-}MOF} : M_{2\text{-aminoterephthalic acid}} = 1 : 1$) was dissolved in DMF and quickly poured into the flask, which was heated at 200 °C for 2 h to allow the nitrogen-containing structural units to be fully absorbed by the MOF clusters. The subsequent preparation of $SnSe_2$/C–N was carried out in the same way as that of $SnSe_2$/C.

Characterization

First, the microscopic morphologies of the Sn-MOF, $SnSe_2$/C and $SnSe_2$/C–N were observed using an FE-SEM (Field Emission Scanning Electron Microscope, Japan-Hitachi S-4800) and a TEM (Transmission Electron Microscope, Hitachi S-4800, Japan). After that, the main phase compositions and crystal structures of $SnSe_2$/C and $SnSe_2$/C–N were determined using powder XRD (X-ray diffraction: Netherlands X'pert TROMPD (Philips), Cu-Kα radiation). The elemental compositions and the valence of each element in $SnSe_2$/C–N were detected by XPS (X-ray photoelectron spectroscopy, USA-Escalab 250, Al-Kα source). Then to further identify the chemical bonds present in the composites to probe their structure, Fourier Transform Infrared (FT-IR) spectra in the range of 500–3000 cm^{-1} were measured on a Nicolet AVATAR 370 infrared spectrometer. Subsequently, an ICP (Inductively Coupled Plasma, PerkinElmer ICP 2100) test was performed in order to characterize the Sn and Se content in the composites. Afterwards, in order to investigate the proportion of carbon and reactive materials in the composites, the materials were subjected to a temperature increase test by TGA (thermogravimetric analysis, Germany-STA2500, temperature increase rate: 10 °C min^{-1}, temperature range: 25–800 °C). Finally, the adsorption–desorption curves of N_2 were tested with a Micromeritics analyzer (USA-ASAP 2460, exhaust temperature: 473 k). The specific surface area (m^2 g^{-1}) and pore size (nm) distribution of the samples were calculated utilizing the BET equation and BJH method.

Electrochemical measurements

The electrochemical properties of the samples have been investigated with a semi-cell. The working electrode is composed of an active material (weight ratio: 70%), acetylene black (weight ratio: 20%) and polyvinylidene fluoride (weight ratio: 10%, PVDF). The above substances were proportionally mixed in *N*-methyl-pyrrolidone (NMP) solution and uniformly ground for 5 h. Subsequently, the mixture was coated onto copper foil (1.1 cm^2) and dried under vacuum for 12 h (70 °C) to obtain the working electrode in which the active material (*e.g.* $SnSe_2$/C–N) loading was 1.0–1.5 mg cm^{-1}. Lithium foil and a polypropylene film were used as the reference electrode material and diaphragm for the CR2032 LIB half-cell, respectively. The electrolyte consisted of dimethyl carbonate (DMC) and ethylene carbonate (EC) dissolved (V/V, 1 : 1) in 1 M $LiPF_6$. The sodium-ion button cell used for the charge/discharge tests had a sodium metal foil as the standard comparison electrode, and the electrolyte consisted of 1 M $NaClO_4$ in ethylene carbonate (EC) and diethyl ethyl carbonate (DEC) (V/V, 1 : 1) with a 2% additive of fluoroethyl bicarbonate (FEC). The batteries were constructed in a glove box under standard conditions (H_2O, O_2 < 0.1 ppm). The electrochemical properties of the material were tested on the CT-3008 system (China-Neware, voltage window: 0.01–3 V) and they included charge/discharge curves, cycling performance, and rate performance. Cyclic voltammetry (CV, scan rate: 0.1 mV s^{-1}) and electrochemical impedance spectroscopy (EIS, parameter setting, frequency: 0.01–100 kHz; voltage disturbance: 5 mV) were performed in electrochemical workstations (China-CHI660D). All the above activity data were calculated from the total quality of the electrodes. In addition, the electrostatic energies and binding energies at the active sites during the binding process of $SnSe_2$/C and $SnSe_2$/C–N with Li/Na were simulated using Gaussian 16. The reagents and their products were further optimized at the B3LYP-D3BJ/Def2-SVP level, using Density Functional theory (DFT) methods.[73]

Results and discussion

Synthesis and characterization

As shown in Fig. 1a, the Sn-MOF precursor and two electrode samples required for the experiments were prepared by hydrothermal and calcination methods, respectively, using $SnSe_2$/C–N as an example. The morphologies and microstructures of Sn-MOF, $SnSe_2$/C, and $SnSe_2$/C–N were characterized by SEM as shown in Fig. 1b–d. The Sn-MOF clearly exhibits a relatively homogeneous hexahedral structure (Fig. 1b), with a diameter

Published on 11 July 2024. Downloaded on 4/29/2026 2:52:14 AM.

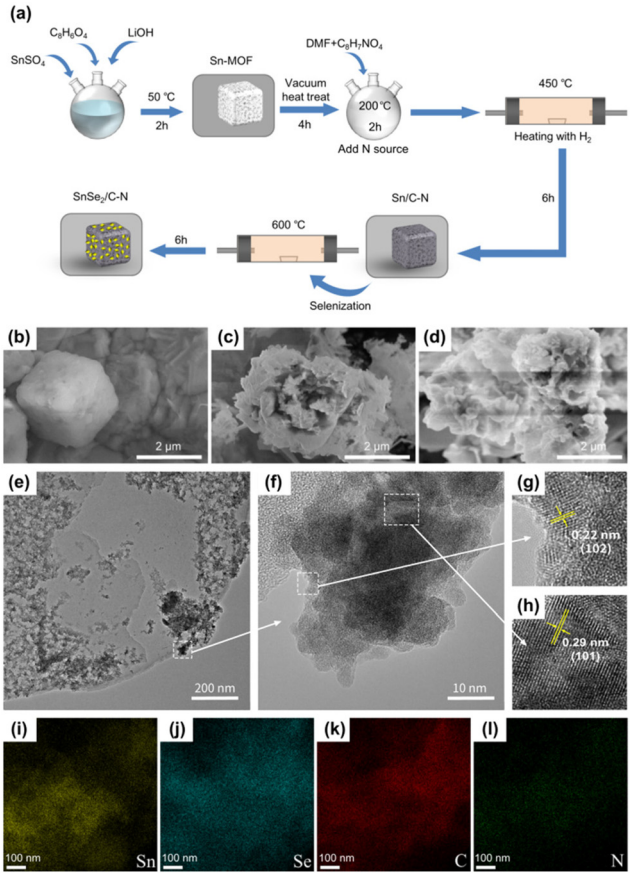

Fig. 1 (a) The schematic representation of the $SnSe_2$/C–N process; SEM images: (b) Sn-MOF, (c) $SnSe_2$/C, and (d) $SnSe_2$/C–N; (e) TEM image of $SnSe_2$/C–N; (f), (g) and (h) HRTEM images of $SnSe_2$/C–N; and EDS mapping images for $SnSe_2$/C–N: (i) Sn, (j) Se, (k) C and (l) N.

of about 1.5–1.8 μm. The SEM images of $SnSe_2$/C after vacuum selenization (Fig. 1c and d) show that it inherits the hexahedral structure of the Sn-MOF and forms a number of thin layers of $SnSe_2$ nanosheets with irregular thickness clusters on the hexahedral surface. The SEM images of $SnSe_2$/C–N (Fig. 1d) confirm that the Sn-MOF doped with nitrogen by the implantation method formed a structure similar to that of $SnSe_2$/C after vacuum vulcanization, which indicates that the doping of $C_8H_7NO_4$ does not affect the formation of the $SnSe_2$ composite structure. Unlike $SnSe_2$/C, the size and morphology of the nanosheets on the surface of the material are different. From the comparison, it can be clearly seen that the thickness of nanosheets relatively increases after doping with $C_8H_7NO_4$ and slight agglomeration occurs. Fig. S1† shows the SEM image of $SnSe_2$/C–N after 100 cycles of charge/discharge (LIBs), which indicates that the skeleton structure of the material can still be preserved intact even after several reactive ion (de-)/intercalations, confirming the reason for its long cycling stability. The deeper microstructure and crystalline morphology of the $SnSe_2$/C–N composites were characterised by TEM, as shown in Fig. 1e–h. The clearly visible lattice stripes from the HRTEM images (Fig. 1f–h) proved that the $SnSe_2$ nanocomplexes have excellent crystal properties with spacings of 0.29 and 0.22 nm, which correspond to the (101) and (102) planes of the standard $SnSe_2$ as determined by XRD. In addition, Fig. 1i–l and Fig. S2† reflect the elemental mapping analysis of the composites. The results confirm that the composites contain Sn, Se, N and C elements, and the distribution of each element is uniform and clearly visible, which indicates that the carbon coating in the composite structure is well preserved and not damaged during calcination at 600 °C. Comparing the images with different colours, the Sn and Se elements are uniformly dispersed in the selected areas without agglomeration, further proving the dispersion of $SnSe_2$ nanoparticles.

The crystallinities of the samples were characterized using XRD. Fig. 2a shows the XRD patterns of the Sn-MOF, $SnSe_2$/C and $SnSe_2$/C–N. Sharp peaks of $SnSe_2$ can be clearly seen in the test data plot lines, while the carbon skeleton does not show any distinct peaks, indicating that the C and C–N skeletons in the sample are amorphous. In addition, all the sharp diffraction peaks of $SnSe_2$/C and $SnSe_2$/C–N are consistent with those of the original $SnSe_2$ standard materials (JCPDS #23-0602). It can be seen that the diffraction peaks of the Sn-MOF are accurate and distinct,[74] and the diffraction peaks of $SnSe_2$/C and $SnSe_2$/C–N samples are not consistent with that of the Sn-MOF, which suggests that the composite samples are well-crystallized and free of impurity components.

To investigate the structural composition of the amorphous part of the composites, $SnSe_2$/C and $SnSe_2$/C–N composites were characterized using FTIR (Fig. S3†). The characteristic

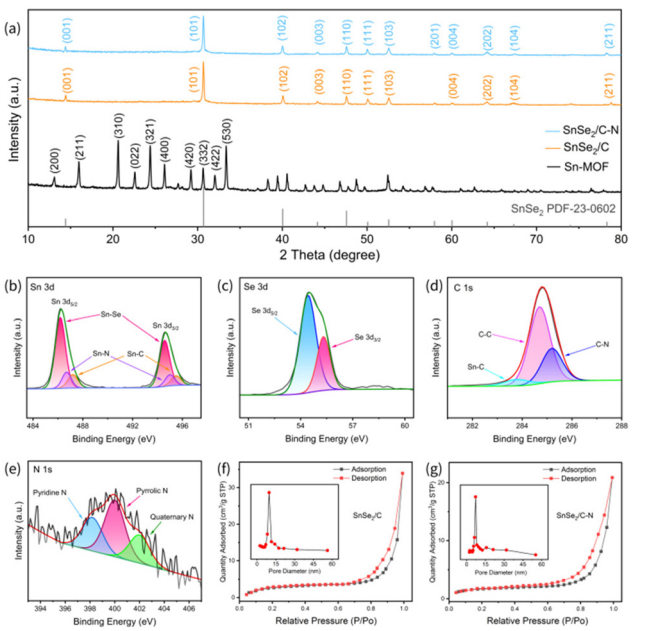

Fig. 2 (a) XRD patterns of the Sn-MOF, $SnSe_2$/C and $SnSe_2$/C–N composites; XPS analysis of (b) Sn 3d, (c) Se 2p, (d) C 1s, and (e) N 1s in $SnSe_2$/C–N; and N_2 adsorption (desorption) isotherms and pore size distributions for (f) $SnSe_2$/C and (g) $SnSe_2$/C–N.

This journal is © The Royal Society of Chemistry 2024

Published on 11 July 2024. Downloaded on 4/29/2026 2:52:14 AM.

peak at 1558 cm^{-1} common to both composites is attributed to the C–C stretching vibration.[75,76] In addition, the characteristic peaks of $SnSe_2$/C–N observed in the spectral bands 1408 cm^{-1} and 1252 cm^{-1} are then related to the C–N stretching vibration, confirming the presence of nitrogen-doped carbon, which promotes the electron mobility.[77–79] The obtained results indicate that the prepared $SnSe_2$/C and $SnSe_2$/C–N composites exhibit characteristic vibrations with the expected structures, which further proves the successful synthesis of nitrogen-doped carbon skeletons.[80] Regarding the ICP test, we tested and analyzed the Sn and Se elements in the $SnSe_2$/C–N samples, and the test results showed that the mass percentage of the Sn element was 29.62%, while that of the Se element was 39.11%, which corresponds to an atomic number ratio of Sn : Se of about 1 : 2.

Fig. 2b–e and Fig. S4† show the XPS spectra of the $SnSe_2$/C–N composite, mainly to analyze the chemical state of the sample surface in more depth. The presence of C, N, Sn and Se in the composites can be confirmed from Fig. S4.† Quantitative analysis of the elements C, N, Sn, and Se in the samples based on XPS peak area calculations showed that the surface atomic concentrations were 81.55%, 0.08%, 12.14%, and 6.23%, respectively, indicating that the atomic ratios of Sn to Se were around 1 : 2, and it proves the conclusion of nitrogen doping. In addition, the elemental binding behavior in the $SnSe_2$/C–N samples can be evaluated by high-resolution XPS of the N 1s, Se 3d and Sn 3d regions. As can be seen from the high-resolution XPS results of Sn 3d in Fig. 2b, the two major peaks at 486.2 eV and 494.6 eV correspond to $3d_{5/2}$ and $3d_{3/2}$, respectively, which confirms the presence of Sn–Se.[81,82] The two additional peaks in Fig. 2b at 487.2 and 495.6 eV can be assigned to Sn–C bonds,[83,84] and the peaks in Fig. 2b at 486.7 and 495.1 eV can be attributed to Sn–N bonds,[85,86] respectively. The peak in the Se 3d spectrum (Fig. 2c) can recoil into two smaller peaks, which are formed mainly by the higher peaks at 55.3 eV and 56.2 eV corresponding to the $3d_{5/2}$ and $3d_{3/2}$ binding energies of Se.[82,87] In the XPS spectra of C1s (Fig. 2d), the peaks at 283.5 eV, 284.5 eV and 285.3 eV correspond to Sn–C, C–C and C–N, respectively.[88,89] Finally, the peaks of 398.2 eV, 400.0 eV and 402.0 eV in the N1s spectrum (Fig. 2e) correspond to pyridine-N, pyrrole-N and quaternary-N, respectively.[30,52,90] In addition, previous studies have demonstrated that the introduction of pyrrole nitrogen in carbon layers improves the electrical conductivity and creates structural defects to form active sites for Li^+ intercalation.[65] To further determine the content of $SnSe_2$ and C in the composites, TGA tests were performed on $SnSe_2$/C and $SnSe_2$/C–N materials under an air atmosphere at a heating rate of 10 °C min^{-1}, and the results are shown in Fig. S5.† In the case of $SnSe_2$/C, for example, the decomposition and oxidation of $SnSe_2$ and sublimation of SeO_2 occur at temperatures above 300 °C, resulting in a sharp weight loss. The weight loss between 650 °C and 800 °C is due to carbon combustion.[91] Therefore, the content of C and $SnSe_2$ in the $SnSe_2$/C composite can be calculated to be approximately 35.7% and 64.3%, respectively. Following the same calculation method, the contents of C and $SnSe_2$ in $SnSe_2$/C–N can be calculated to be about 36.2% and 63.8%, respectively. This further confirms that the injected organic ligands have been successfully introduced into the MOF cluster structure and completely dehydrogenated into N-containing carbon skeletons during the subsequent hydrogen calcination and vacuum selenization processes. By analyzing the nitrogen adsorption–desorption curves, the specific surface area and pore size assignments of $SnSe_2$/C–N and $SnSe_2$/C were obtained as shown in Fig. 2f and g. The BET specific surface areas of $SnSe_2$/C and $SnSe_2$/C–N were 12.85 $m^2\ g^{-1}$ (average pore size: 11.3 nm) and 6.76 $m^2\ g^{-1}$ (average pore size: 8.8 nm), respectively. The isothermal curves follow the characteristics of mesoporous materials.[92] According to the above data, the metal ions are connected to the lone pair of electrons of N through ligand bonds, and N generates a carbon coating during vacuum carbonization. This carbon partially clogs or closes the Sn-MOF pores, resulting in a decrease in the specific surface area.

Electrochemical performance

$SnSe_2$/C–N for LIBs. After cyclic voltammetry testing of LIBs with $SnSe_2$/C–N anodes at a scan rate of 0.1 mV s^{-1} and a

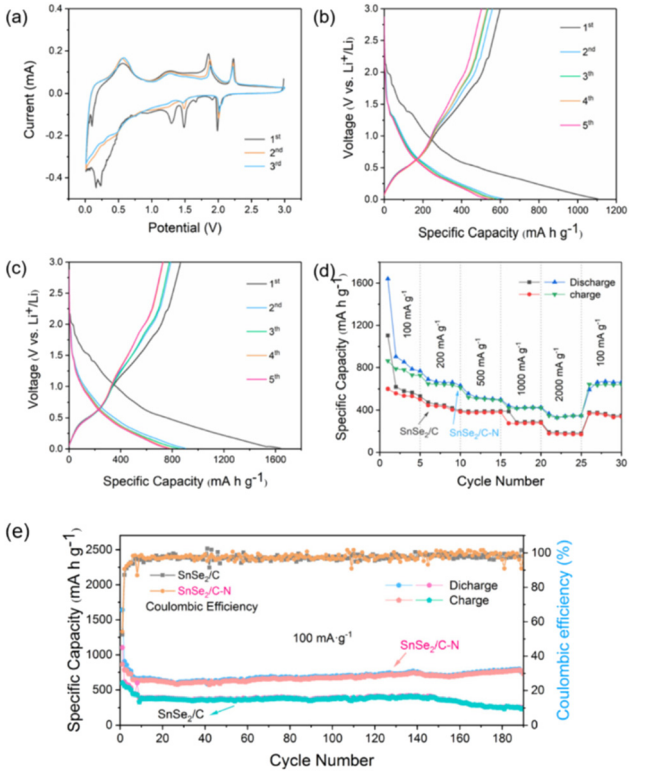

Fig. 3 (a) CV curves of $SnSe_2$/C–N at 100 mV s^{-1}Constant current charge (discharge) curves at 100 mA g^{-1} of (b) $SnSe_2$/C and (c) $SnSe_2$/C–N. (d) Rate performance and charge (discharge) profiles of $SnSe_2$/C-NB at different rates. (e) Performance of all electrodes for cycling at 100 mA h g^{-1}.

Published on 11 July 2024. Downloaded on 4/29/2026 2:52:14 AM.

scan voltage range of 0.01–3 V, the resulting CV curves (Fig. 3a) show the following electrochemical reaction processes:[91,93,94]

$$SnSe_2 + 4Li^+ + 4e^- \rightarrow Sn + 2Li_2Se \quad (1)$$

$$Sn + xLi^+ + xe^- \leftrightarrow Li_xSn(0 < x \ll 4.4) \quad (2)$$

During the first cathodic scan, lithiation begins with a reduction peak at ~1.98 V, marking the initial insertion of Li^+. The sharp reduction peak at ~1.48 V is attributed to the formation of Sn and Li_2Se from $SnSe_2$ *via* a conversion reaction (eqn (1)). The sharp reduction peak at ~1.29 V is irreversible due to the formation of a solid–electrolyte interface (SEI) film. In addition, the reduction peak between 0.3 V and 0.01 V is attributed to the alloying reaction of Sn with Li^+ (eqn (2)).[91] For the first anodic scan, the oxidation peaks between 0.5 V and 0.6 V were attributed to the dealloying process of Li_xSn and the oxidation peaks at ~1.85 and ~2.22 V corresponded to the decomposition of Li_2Se and the oxidation of Sn to $SnSe_2$, respectively (eqn (1)). In subsequent cycles, the redox pairs at ~0.56/0.25 V are assigned to the dealloying/alloying between Li and Sn, whereas the redox pairs at ~1.87/1.49 V and ~2.22/1.99 V come from the reversible conversion of $SnSe_2$ and Li_2Se. The intensity of these peaks remains constant, implying highly reversible Se alloying/dealloying and conversion reactions.[93]

The initial and reversible specific capacity obtained from charging/discharging tests is one of the important indexes for evaluating the energy storage characteristics of batteries. The specific capacity obtained under the same current density is a very intuitive evaluation standard, and the performance of the battery is positively correlated with this data. The constant current charge and discharge curves when $SnSe_2$/C and $SnSe_2$/C–N are used as anode materials for LIBs are shown in Fig. 3b and c. The initial discharge capacities of $SnSe_2$/C and $SnSe_2$/C–N materials are 1110.67 mA h g^{-1} and 1621.94 mA h g^{-1}, and it can be clearly seen that the latter has a higher initial specific capacity. The charging capacity values are 600.1 and 849.7 mA h g^{-1}, and the initial coulombic efficiency (ICE) values are 54.5% and 53.1% respectively. As shown in Fig. 3d, the average specific capacity of discharge at different current densities exhibited 793.0, 655.5, 503.2, 347.7, and 166.0 mA h g^{-1} for the cycling tests at 100, 200, 500, 1000, and 2000 mA g^{-1}, respectively. Back to 100 mA g^{-1}, $SnSe_2$/C–N still show an impressive reversible specific capacity (662.1 mA h g^{-1}), and the capacity retention of 83.5% indicates its good rate performance. In terms of long cycle life testing (Fig. 3e), it can maintain a reversible capacity of 695 mA h g^{-1} after 100 cycles. It is worth mentioning that its reversible specific capacity has the tendency to continuously increase and subsequently level off during the subsequent cycling process, even rising to 791.4 mA h g^{-1} after 200 cycles. This may be caused by the gradual activation of the composite nanoparticles during the cycling process which improves the Li^+ diffusion rate.[95]

The $SnSe_2$/C–N anode material can exhibit extremely high reversible capacity and excellent rate performance for the following reasons: firstly, the MOF-derived carbon skeleton has good electrical conductivity, which leads to a greatly enhanced electrochemical reaction rate of the electrode material. In addition, the pretreatment of the MOF with the organic nitrogen source resulted in the introduction of nitrogen on the surface of the final sample nanosheets, which not only increased the stability of the intrinsic carbon skeleton of the MOF, but also brought more active sites for chemical reactions. In order to reflect the dynamics of the $SnSe_2$/C and $SnSe_2$/C–N charge transfer processes at room temperature, the composites were subjected to Electrochemical Impedance Spectroscopy (EIS) tests. The Nyquist equivalent circuit diagrams fitted to the curves are shown in Fig. S6† and each diagram consists of four parts. Initially, the SEI surface resistance (R_s) corresponds to a compressed semicircle in the high frequency region. In addition, the semicircle in both the mid-frequency and low-frequency domains corresponds to the charge transfer resistance (R_{ct}) of the unit system.[96] Equivalent circuit fitting results show that $SnSe_2$/C–N (27.1 Ω) has a lower R_{ct} value compared to $SnSe_2$/C (57.3 Ω). The lower R_{ct} value of the $SnSe_2$/C–N anode suggests that the nitrogen-doped skeleton further enhances the solid-state diffusion rate of Li^+ inside the electrode as compared to that of the pristine carbon skeleton.[97]

In addition, the pseudocapacitive contribution to the lithium storage capacity was also dynamically analyzed, since the charge storage mechanism of the energy storage system is divided into diffusion control and capacitance control. The quantitative analysis was performed based on i (peak current) and v (scan rate) in eqn (3), where a and b are random parameters. When b approaches 0.5, the electrochemical response tends to be generated by diffusion control contribution, whereas when b is closer to 1, it tends to be generated more by capacitive control contribution.[15,98–100] The b-values corresponding to the five peaks were calculated by linearly fitting the log(i) *versus* log(v) curves (eqn (4)). The b-values for each redox peak are 0.90, 0.80, 0.81, 0.99, and 0.91, respectively (Fig. 4b),

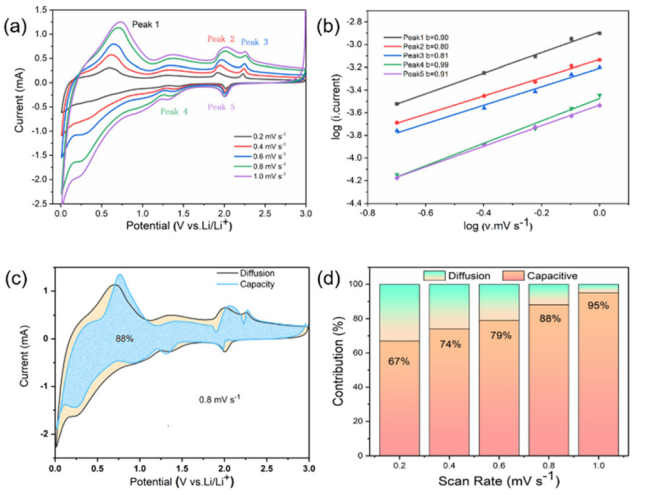

Fig. 4 (a) CV curves of $SnSe_2$/C–N for different scan rates (0.2–1.0 mV s^{-1}), (b) log(scan rate)/log(current) plots, (c) pseudocapacitive contribution (orange area) at 0.8 mV s^{-1}, and (d) histogram of the pseudocapacitive contributions at different scan rates.

This journal is © The Royal Society of Chemistry 2024

Published on 11 July 2024. Downloaded on 4/29/2026 2:52:14 AM.

which suggests that capacitance control dominates the charge storage mechanism of the material.

$$i = a \cdot v^b \quad (3)$$

$$\log(i) = b \cdot \log(v) + \log(a) \quad (4)$$

$$i = k_1 v + k_2 v^{1/2} \quad (5)$$

The specific contributions of capacitive control ($k_1 v$) and diffusion control ($k_2 v^{1/2}$) values were calculated by graphical fitting of eqn (5). For example, the capacitive control of $SnSe_2$/C–N contributes 88% at 0.8 mV s^{-1} (Fig. 4c) and as the scan rate increases from 0.2 to 1.0 mV s^{-1}, its capacitance contribution increases sequentially from 67% to 95%. As a comparison, the capacitance contribution of the undoped $SnSe_2$/C composite is much lower than that of $SnSe_2$/C as can be seen in Fig. S7,† which indicates that the high mass transfer conductivity of the nitrogen-doped carbon skeleton composites is further verified.[101,102]

$SnSe_2$/C–N for SIBs. The prepared $SnSe_2$/C–N composites were also used as anodes for SIBs for additional studies (Fig. 5). Fig. 5a shows the CV plot lines for the first three cycles of the $SnSe_2$/C–N electrode. From the plots, it could be analyzed that the sodium storage reaction mechanism of $SnSe_2$ can be represented by the following two basic steps:[103]

$$SnSe_2 + 4Na^+ + 4e^- \rightarrow Sn + 2Na_2Se \quad (6)$$

$$Sn + 3.75Na^+ + 3.75e^- \leftrightarrow Na_{3.75}Sn \quad (7)$$

A reversible reduction peak around 1.0–1.2 V was detected in the first cathodic scan, which can be attributed to the generation of Sn with Na_2Se (eqn (6)). The peaks around 0.5–0.7 V are due to the alloying reaction to produce $Na_{3.75}Sn$ (eqn (7)). The two anodic peaks around 1.61 V and 2.12 V are clearly visible in the subsequent anodic scans, and they correspond to phase transitions during the dealloying process and the re-oxidation of Sn. Fig. 5b and c exhibit the charge–discharge curves of the two composites in the voltage range of 0.01–0.3 V and 100 mA g^{-1} for investigating the electrochemical performance of the materials in SIB anode applications. The initial discharge/charge capacities of $SnSe_2$/C–N are 1092.1 mA h g^{-1} and 421.4 mA h g^{-1}, while the corresponding initial capacities of $SnSe_2$/C are only 570.2 mA h g^{-1} and 200.1 mA h g^{-1}. The SIBs were tested for rate and cycling performance at the same current density settings as the LIBs in the previous subsection (Fig. 5d and e). As shown in Fig. 5e, the $SnSe_2$/C–N electrode achieves a good reversible specific capacity (271 mA h g^{-1}) after 100 cycles at 100 mA g^{-1}. The temperature difference between day and night during the testing of $SnSe_2$/C–N materials may lead to capacity fluctuations. In addition, the Coulombic Efficiency (CE) for $SnSe_2$/C–N materials was stable at around 100%, indicating that the interface between the $SnSe_2$/C–N electrodes and the electrolyte can be stabilized for a long time. Therefore, it can be proved that the electrochemical reaction of $SnSe_2$/C–N is highly stable and reversible.[73]

The dynamic testing and subsequent analysis of the SIBs were performed with the same parameter settings as for the LIBs (Fig. 6). According to the calculation results in Fig. 6b, the ionic contribution in SIBs is dominated by diffusion. For example, at a scan rate of 0.4 mV s^{-1}, the capacitance control contribution is 50.9% based on the fitted plot line (Fig. 6c).

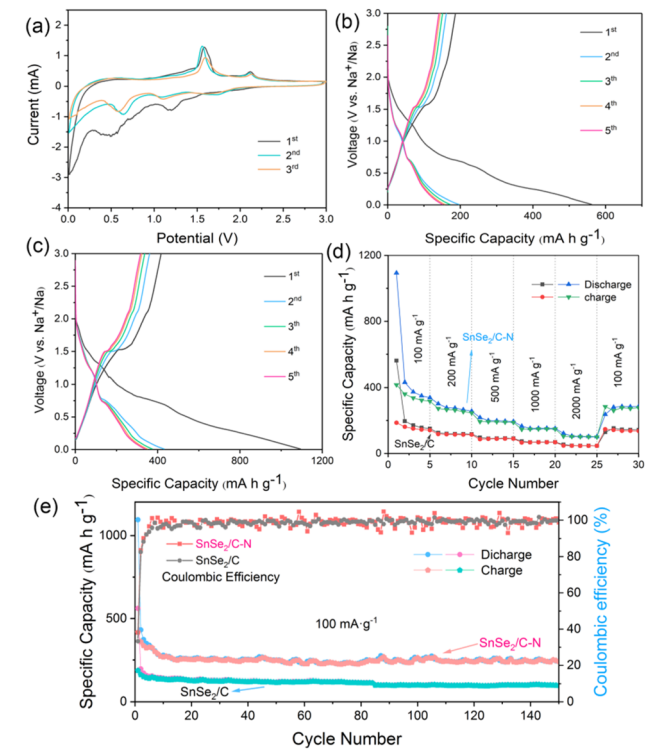

Fig. 5 (a) CV curves of $SnSe_2$/C–N at 0.1 mV s^{-1}; constant current charge/discharge curves of (b) $SnSe_2$/C and (c) $SnSe_2$/C–N at 0.1 A g^{-1}; (d) rate performance of $SnSe_2$/C, and $SnSe_2$/C–N electrodes at different rates; and (e) cycling performance at 0.1 A g^{-1}.

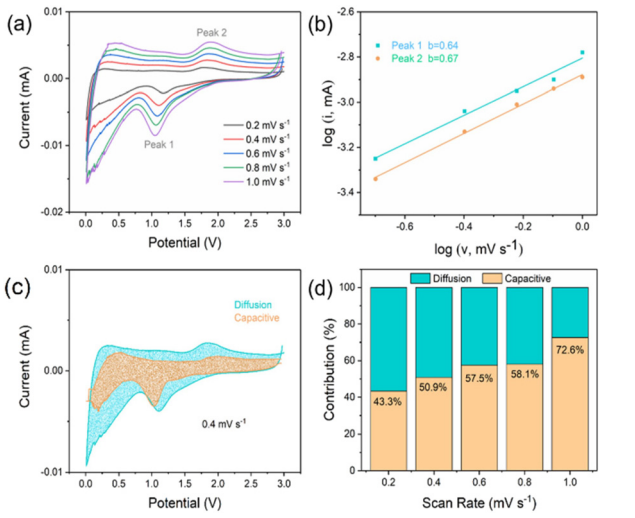

Fig. 6 (a) CV of $SnSe_2$/C–N curves for different scan rates (0.2–1.0 mV s^{-1}), (b) log(scan rate)/log(current) plots, (c) pseudocapacitive contribution (orange area) at 1.0 mV s^{-1}, and (d) histogram of the pseudocapacitive contributions at different scan rates.

Published on 11 July 2024. Downloaded on 4/29/2026 2:52:14 AM.

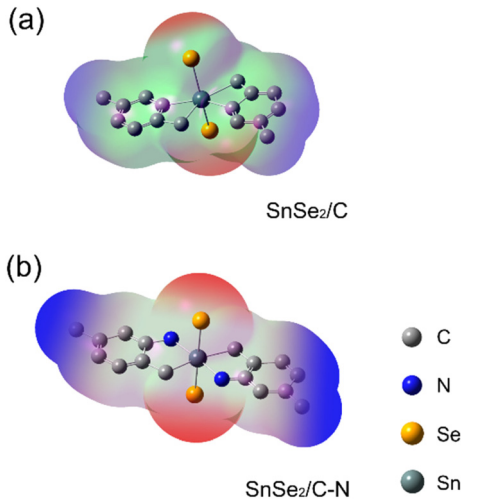

Fig. 7 Molecular surface electrostatic energy of (a) $SnSe_2$/C and (b) $SnSe_2$/C–N using Gaussian 16.

However, it can be seen from Fig. 6d that the capacitance contribution increases from 43.3% to 72.6% as the scan rate increases (0.2 to 1.0 mV s^{-1}), indicating that the effect of nitrogen doping on the carbon skeleton in the SIB application has a similar gain to that in the LIBs.

DFT calculations. The surface electrostatic energies of $SnSe_2$/C and $SnSe_2$/C–N were obtained using Gaussian 16, as shown in Fig. 7. The red region with a negative electrostatic potential implies a more nucleophilic region that is more likely to give electrons compared to the other regions; in contrast, the one in the blue region implies a positive electrostatic potential that is more electrophilic.[104] By comparing $SnSe_2$/C with $SnSe_2$/C–N, it is clear that $SnSe_2$/C–N displays a larger red-blue area, which suggests that $SnSe_2$/C–N is more likely to exhibit better electrochemical properties through a higher affinity for Li^+/Na^+ or electrons.

The binding energies of $SnSe_2$/C and $SnSe_2$/C–N after the attack of the active site by Li in $SnSe_2$/C–N were also specifically calculated using Gaussian 16, and the results are shown in Table 1. Using Li with $SnSe_2$/C as an example, the adsorption capacity of $SnSe_2$/C and $SnSe_2$/C–N for Li^+/Na^+ was explored according to the following equation: $E_{bind} = E_{Li\text{-}SnSe_2/C} - E_{SnSe_2/C} - E_{Li}$. In the comprehensive analysis, the larger nucleophilic/electrophilic region of the electrostatic potential energy of the molecular surface of $SnSe_2$/C–N enhances its ability to attract more Li^+/Na^+ and electrons, which promotes the electrochemical process. Furthermore, the smaller binding energy of $SnSe_2$/C–N with Li^+/Na^+ also indicates the higher reversible specific capacity during long cycling.

Table 1 Theoretical calculations of simulated binding energy

Different category	E (Hatree)	E_{bind} (Hatree)
Li	−7.4909023	—
Na	−162.2866299	—
$SnSe_2$/C	−5414.9401514	—
$SnSe_2$/C–N	−5524.4772155	—
Li with $SnSe_2$/C	−5421.2881263	1.1429274
Li with $SnSe_2$/C–N	−5531.8693801	0.0987377
Na with $SnSe_2$/C	−5576.1884092	1.0383721
Na with $SnSe_2$/C–N	−5686.5860736	0.1777718

Conclusions

In this work, the Sn-MOF-derived $SnSe_2$/C–N anode materials synthesized after nitrogen doping modification showed excellent rate and cycling performance for both LIB and SIB applications, with reversible capacities of 695 mA h g^{-1} and 259 mA h g^{-1} after 100 cycles at 100 mA g^{-1}, respectively. This work has the following breakthroughs compared to other studies: firstly, the innovative concept of using MOFs as precursors was utilized to form $SnSe_2$/C–N composites by hydrogen reduction, resulting in a stable carbon framework. Secondly, the carbon skeleton inherited from the Sn-MOF precursor can further improve the electrical conductivity of the $SnSe_2$/C–N materials, effectively improving the multiplicity and cycling performance of the electrode material. Thirdly, the modification of the Sn-MOF by using nitrogen-containing organic ligands in the MOF clusters enhances the mechanical properties of the carbon skeleton, which further improves the stability of the Li^+/Na^+ storage skeleton in the $SnSe_2$/C–N materials. Finally, the successful application of $SnSe_2$/C–N materials modified by N-doping only by a simple process in SIBs demonstrates that there is still much room for exploring the potential of Sn-based anode materials in SIBs, and our work will provide new ideas for the application of other N-doped materials in SIBs.

Author contributions

L. Jiang, A. L. Song, B. H. J. Tang, and H. Tian designed and supervised the study; Z. Y. Chen and Z. Zhang synthesized the samples, analysed the data and wrote the manuscript; L. Z. Wang, Y. F. Li, and Y. T. Wang performed the DFT calculations; Y. C. Rui characterized the structure; A. L. Song, M. Li, Y. Y. Xiang and K. B. Chou recorded the XRD and XPS spectra; N. Han and G. X. Wang proofread this manuscript. All authors discussed and commented on the manuscript.

Data availability

The data that support the findings of this study are available on request from the corresponding authors.

Conflicts of interest

There are no conflicts to declare.

This journal is © The Royal Society of Chemistry 2024

Published on 11 July 2024. Downloaded on 4/29/2026 2:52:14 AM.

Acknowledgements

This work was supported by the National Natural Science Foundation of China (52202178), Natural Science Foundation of Shanghai (22ZR1426300), and Class III Peak Discipline of Shanghai-Materials Science and Engineering (High-Energy Beam Intelligent Processing and Green Manufacturing). The authors extend their gratitude to Mr Yang Junjie from Shiyanjia Lab (**https://www.shiyanjia.com**) for providing invaluable assistance with the BET analysis.

References

1 D. J. Wuebbles and A. K. Jain, *Fuel Process. Technol.*, 2001, **71**, 99–119.
2 X. B. Cheng, H. Liu, H. Yuan, H. J. Peng, C. Tang, J. Q. Huang and Q. Zhang, *SusMat*, 2021, **1**, 38–50.
3 K. B. Chin, E. J. Brandon, R. V. Bugga, M. C. Smart, S. C. Jones, F. C. Krause, W. C. West and G. G. Bolotin, *Proc. IEEE*, 2018, **106**, 419–428.
4 B. Crew, *Nature*, 2022, **609**, S1–S1.
5 W. A. Braff, J. M. Mueller and J. E. Trancik, *Nat. Clim. Change*, 2016, **6**, 964–969.
6 M. S. Ziegler, *Joule*, 2021, **5**, 1925–1927.
7 J. M. Amanor-Boadu, M. A. Abouzied and E. Sánchez-Sinencio, *IEEE Trans. Ind. Electron.*, 2018, **65**, 7383–7394.
8 J. Li, Z. Du, R. E. Ruther, S. J. An, L. A. David, K. Hays, M. Wood, N. D. Phillip, Y. Sheng and C. Mao, *JOM*, 2017, **69**, 1484–1496.
9 T. S. Pathan, M. Rashid, M. Walker, W. D. Widanage and E. Kendrick, *JPhys Energy*, 2019, **1**, 044003.
10 J. Wang, Q. Zheng, M. Fang, S. Ko, Y. Yamada and A. Yamada, *Adv. Sci.*, 2021, **8**, 2101646.
11 M. Fan, X. Chang, Q. Meng, L. J. Wan and Y. G. Guo, *SusMat*, 2021, **1**, 241–254.
12 R. A. House, U. Maitra, M. A. Pérez-Osorio, J. G. Lozano, L. Jin, J. W. Somerville, L. C. Duda, A. Nag, A. Walters and K.-J. Zhou, *Nature*, 2020, **577**, 502–508.
13 C. Wang, G. Zhang, S. Ge, T. Xu, Y. Ji, X. Yang and Y. Leng, *Nature*, 2016, **529**, 515–518.
14 C.-Y. Wang, T. Liu, X.-G. Yang, S. Ge, N. V. Stanley, E. S. Rountree, Y. Leng and B. D. McCarthy, *Nature*, 2022, **611**, 485–490.
15 J. He, C. Lu, H. Jiang, F. Han, X. Shi, J. Wu, L. Wang, T. Chen, J. Wang and Y. Zhang, *Nature*, 2021, **597**, 57–63.
16 K. J. Griffith, K. M. Wiaderek, G. Cibin, L. E. Marbella and C. P. Grey, *Nature*, 2018, **559**, 556–563.
17 Z. Liao, S. Zhang, K. Li, G. Zhang and T. G. Habetler, *J. Power Sources*, 2019, **436**, 226879.
18 J. Darga, J. Lamb and A. Manthiram, *Energy Technol.*, 2020, **8**, 2000723.
19 F. Xie, L. Zhang, C. Ye, M. Jaroniec and S. Z. Qiao, *Adv. Mater.*, 2019, **31**, 1800492.
20 Q. Bai, L. Yang, H. Chen and Y. Mo, *Adv. Energy Mater.*, 2018, **8**, 1702998.
21 N. Yabuuchi, K. Kubota, M. Dahbi and S. Komaba, *Chem. Rev.*, 2014, **114**, 11636–11682.
22 H. Tian, A. Song, H. Tian, J. Liu, G. Shao, H. Liu and G. Wang, *Chem. Sci.*, 2021, **12**, 7656–7676.
23 J. Chai, N. Han, S. Feng, X. Huang, B. Tang and W. Zhang, *Chem. Eng. J.*, 2023, **453**, 139768.
24 J. Liu, D. Xie, W. Shi and P. Cheng, *Chem. Soc. Rev.*, 2020, **49**, 1624–1642.
25 Y. Ma, Y. Ma, G. T. Kim, T. Diemant, R. J. Behm, D. Geiger, U. Kaiser, A. Varzi and S. Passerini, *Adv. Energy Mater.*, 2019, **9**, 1902077.
26 P. Lou, Z. Cui, Z. Jia, J. Sun, Y. Tan and X. Guo, *ACS Nano*, 2017, **11**, 3705–3715.
27 L. Wang, Q. Li, Z. Chen, Y. Wang, Y. Li, J. Chai, N. Han, B. Tang, Y. Rui and L. Jiang, *Small*, 2024, 2310426.
28 J. Du, Q. Li, J. Chai, L. Jiang, Q. Zhang, N. Han, W. Zhang and B. Tang, *Dalton Trans.*, 2022, **51**, 9584–9590.
29 Y. Gong, Y. Li, Y. Li, M. Liu, Y. Bai and C. Wu, *Small*, 2023, **19**, 2206194.
30 H. Tian, H. Tian, S. Wang, S. Chen, F. Zhang, L. Song, H. Liu, J. Liu and G. Wang, *Nat. Commun.*, 2020, **11**, 5025.
31 H. Tan, Y. Feng, X. Rui, Y. Yu and S. Huang, *Small Methods*, 2020, **4**, 1900563.
32 R. Nkum, A. Adimado and H. Totoe, *Mater. Sci. Eng., B*, 1998, **55**, 102–108.
33 W. Yang, Y. Chen, X. Yin, X. Lai, J. Wang and J. Jian, *ACS Appl. Mater. Interfaces*, 2023, **15**, 42811–42822.
34 Z. Zhang, X. Zhao and J. Li, *Electrochim. Acta*, 2015, **176**, 1296–1301.
35 Y. Kim, Y. Kim, Y. Park, Y. N. Jo, Y.-J. Kim, N.-S. Choi and K. T. Lee, *Chem. Commun.*, 2015, **51**, 50–53.
36 Z. Wei, L. Wang, M. Zhuo, W. Ni, H. Wang and J. Ma, *J. Mater. Chem. A*, 2018, **6**, 12185–12214.
37 X. Zhao, W. Wang, Z. Hou, X. Fan, G. Wei, Y. Yu, Q. Di, Y. Liu, Z. Quan and J. Zhang, *Inorg. Chem. Front.*, 2019, **6**, 562–565.
38 J. Xia, Y. Yuan, H. Yan, J. Liu, Y. Zhang, L. Liu, S. Zhang, W. Li, X. Yang and H. Shu, *J. Power Sources*, 2020, **449**, 227559.
39 Q. Yu, B. Wang, J. Wang, S. Hu, J. Hu and Y. Li, *Front. Chem.*, 2020, **8**, 590.
40 K. Wang, W. Ye, W. Yin, W. Chai, Y. Rui and B. Tang, *Electrochim. Acta*, 2019, **322**, 134790.
41 X. Li, J. Zheng, C. He, K. Wang, W. Chai, Y. Duan, B. Tang and Y. Rui, *Electrochim. Acta*, 2019, **326**, 134960.
42 G. Chang, X. Yin, S. Shi, Y. Zhao and J. Zhang, *J. Electrochem. Soc.*, 2020, **167**, 140531.
43 L. Jiang, N. Han, T. Luo, Z. Zhang, F. Liang, D. Wu, X. Li, F. Liu, Y. Rui and W. Zhang, *Chem. Eng. J.*, 2023, **458**, 141451.
44 L. Jiang, W. Yin, C. He, T. Luo, Y. Rui and B. Tang, *Colloids Surf., A*, 2022, **644**, 128843.
45 H. Tian, J. Liang and J. Liu, *Adv. Mater.*, 2019, **31**, 1903886.

Published on 11 July 2024. Downloaded on 4/29/2026 2:52:14 AM.

46 H. Tian, F. Huang, Y. Zhu, S. Liu, Y. Han, M. Jaroniec, Q. Yang, H. Liu, G. Q. M. Lu and J. Liu, *Adv. Funct. Mater.*, 2018, **28**, 1801737.
47 H. Tian, H. Tian, W. Yang, F. Zhang, W. Yang, Q. Zhang, Y. Wang, J. Liu, S. R. P. Silva and H. Liu, *Adv. Funct. Mater.*, 2021, **31**, 2101796.
48 Z. Ma, A. Song, Z. Liu, Y. Guo, X. Yang, Q. Li, Y. Fan, L. Dai, H. Tian and X. Qin, *Adv. Funct. Mater.*, 2023, **33**, 2301112.
49 H. Tian, J. Zhao, X. Wang, L. Wang, H. Liu, G. Wang, J. Huang, J. Liu and G. Lu, *Natl. Sci. Rev.*, 2020, **7**, 1647–1655.
50 J. Liang, Y. Jiao, M. Jaroniec and S. Z. Qiao, *Angew. Chem.*, 2012, **124**, 11664–11668.
51 H. Tian, A. Song, P. Zhang, K. Sun, J. Wang, B. Sun, Q. Fan, G. Shao, C. Chen and H. Liu, *Adv. Mater.*, 2023, **35**, 2210714.
52 H. Tian, X. Liu, L. Dong, X. Ren, H. Liu, C. A. H. Price, Y. Li, G. Wang, Q. Yang and J. Liu, *Adv. Sci.*, 2019, **6**, 1900807.
53 J. Zheng, X. Li, C. He, C. Zhou, H. Zhang, B. Tang and Y. Rui, *ChemElectroChem*, 2020, **7**, 782–791.
54 Z. Li, W. Zhang, Y. Tan, J. Hu, S. He, A. Stein and B. Tang, *Electrochim. Acta*, 2016, **214**, 103–109.
55 X. Li, C. He, J. Zheng, W. Ye, W. Yin, B. Tang and Y. Rui, *J. Alloys Compd.*, 2020, **842**, 155605.
56 Y. Xu, T. Yuan, Z. Bian, J. Yang and S. Zheng, *J. Power Sources*, 2020, **453**, 227467.
57 P. García-García, M. Müller and A. Corma, *Chem. Sci.*, 2014, **5**, 2979–3007.
58 Q.-L. Zhu and Q. Xu, *Chem. Soc. Rev.*, 2014, **43**, 5468–5512.
59 L. Zhang, H. Liu, W. Shi and P. Cheng, *Coord. Chem. Rev.*, 2019, **388**, 293–309.
60 L. Chen and Q. Xu, *Matter*, 2019, **1**, 57–89.
61 Q. Li, N. Han, J. Chai, W. Zhang, J. Du, H. Tian, H. Liu, G. Wang and B. Tang, *Energy*, 2023, 128378, DOI: **10.1016/j.energy.2023.128378**.
62 J. H. Na, H. G. Oh, S. Lee and S.-K. Park, *J. Mater. Chem. A*, 2024, **12**, 2848–2855.
63 Z. Bian, A. Li, R. He, H. Song, X. Chen, J. Zhou and Z. Ma, *Electrochim. Acta*, 2018, **289**, 389–396.
64 H. G. Oh and S. K. Park, *Int. J. Energy Res.*, 2022, **46**, 10677–10688.
65 Z. Zhang, L. Jiang, D. Wu, F. Liang, X. Li, Y. Rui and B. Tang, *J. Alloys Compd.*, 2021, **883**, 160834.
66 L. Jiang, F. Liang, Z. Zhang, D. Wu, J. Chai, T. Luo, N. Han, W. Zhang, Y. Rui and B. Tang, *Chem. Eng. J.*, 2022, **433**, 133568.
67 H. G. Oh, S. H. Yang, Y. C. Kang and S. K. Park, *Int. J. Energy Res.*, 2021, **45**, 17738–17748.
68 J. H. Na, Y. C. Kang and S.-K. Park, *Chem. Eng. J.*, 2021, **425**, 131651.
69 L. Wang, Y. Zheng, X. Wang, S. Chen, F. Xu, L. Zuo, J. Wu, L. Sun, Z. Li and H. Hou, *ACS Appl. Mater. Interfaces*, 2014, **6**, 7117–7125.
70 S. Guo, J. Liu, Q. Zhang, Y. Jin and H. Wang, *J. Alloys Compd.*, 2021, **855**, 157538.
71 J. Zhang, Z. Zhao, Z. Xia and L. Dai, *Nat. Nanotechnol.*, 2015, **10**, 444–452.
72 L. Chen, Z. X. Rao, Z. Chen, Z. H. Wu, S. Yang, Z. J. Feng, H. Y. Yang, F. Y. Zeng, X. B. Li, J. Y. Hu and J. T. Huang, *Rare Met.*, 2024, **43**, 1836–1844.
73 Y. Li, Y. Wang, Z. Chen, Q. Li, J. Du, J. Chai, L. Wang, Y. Rui, L. Jiang and B. Tang, *Chem. Eng. J.*, 2023, **476**, 146577.
74 N. Wu, T. Jia, Y. R. Shi, Y. J. Yang, T. H. Li, F. Li and Z. Wang, *Ionics*, 2020, **26**, 1547–1553.
75 H. S. Kim, D. H. Park, Y. B. Lee, D. C. Kim, H. J. Kim, J. Kim and J. Joo, *Synth. Met.*, 2007, **157**, 910–913.
76 B. Tian and G. Zerbi, *J. Chem. Phys.*, 1990, **92**, 3886–3891.
77 Y. Zou, C. Cai, C. Xiang, P. Huang, H. Chu, Z. She, F. Xu, L. Sun and H. B. Kraatz, *Electrochim. Acta*, 2018, **261**, 537–547.
78 B. Cong, S. Sun, B. Wang, C. Lv, J. Zhao, F. Jin, J. Jia and G. Chen, *Chem. Eng. J.*, 2022, **435**, 135185.
79 B. Guo, Y. Yang, Z. Hu, Y. An, Q. Zhang, X. Yang, X. Wang and H. Wu, *Electrochim. Acta*, 2017, **223**, 74–84.
80 W. Xie, X. Yun, D. Lu, W. Song, H. Gao, Q. Guo, Y. Han, H. Wang, P. Xiao and Y. Chen, *ACS Sustainable Chem. Eng.*, 2023, **12**, 375–385.
81 G. Xi, X. Jiao and X. Hu, *Ionics*, 2023, **29**, 119–128.
82 F. Zhang, Y. Shen, M. Shao, Y. Zhang, B. Zheng, J. Wu, W. Zhang, A. Zhu, F. Huo and S. Li, *ACS Appl. Mater. Interfaces*, 2019, **12**, 2346–2353.
83 Y. Chen, Q. Yang, F. Zhou, J. Wu, J. Wang and Y. Li, *Ionics*, 2021, **27**, 3801–3809.
84 J. Tian, Y. Yao, L. Yang, L. Zha, G. Xu, S. Huang, T. Wei, J. Cao and X. Wei, *New J. Chem.*, 2022, **46**, 5848–5860.
85 E. Lewin and J. Patscheider, *J. Alloys Compd.*, 2016, **682**, 42–51.
86 Y. Wu, F. Li, J. Xue and Z. Lv, *Turk. J. Chem.*, 2020, **44**, 393–408.
87 K. Yang, X. Zhang, K. Song, J. Zhang, C. Liu, L. Mi, Y. Wang and W. Chen, *Electrochim. Acta*, 2020, **337**, 135783.
88 D. Gao, Y. Wang, Y. Liu, H. Sun, M. Wu and H. Zhang, *J. Colloid Interface Sci.*, 2019, **538**, 116–124.
89 Y. Cheng, J. Huang, H. Qi, L. Cao, X. Luo, J. Li, Z. Xu and J. Yang, *Nanoscale*, 2017, **9**, 18681–18689.
90 X. Li, J. Li, R. N. Ali, Z. Wang, G. Hu and B. Xiang, *Chem. Eng. J.*, 2019, **368**, 764–771.
91 W. Yao, C. Cai, J. Xiang, L. He, J. Shi, X. Chang, L. Ruan, Z. Chen and Z. Yao, *J. Electron. Mater.*, 2022, **51**, 6654–6662.
92 Y. Zhuang, J. G. Seong, Y. S. Do, H. J. Jo, Z. Cui, J. Lee, Y. M. Lee and M. D. Guiver, *Macromolecules*, 2014, **47**, 3254–3262.
93 Y. Cheng, J. Huang, L. Cao, H. Xie, Y. Wang, Y. Wang, H. Wu, S. Xi and J. Li, *Ionics*, 2020, **26**, 2855–2862.

This journal is © The Royal Society of Chemistry 2024

94 H. Chen, R. Liu, Y. Wu, J. Cao, J. Chen, Y. Hou, Y. Guo, R. Khatoon, L. Chen and Q. Zhang, *Chem. Eng. J.*, 2021, **407**, 126973.
95 F. Zou, X. Hu, Z. Li, L. Qie, C. Hu, R. Zeng, Y. Jiang and Y. Huang, *Adv. Mater.*, 2014, **26**, 6622–6628.
96 B. Sun, Q. Zhang, H. Xiang, F. Han, W. Tang, G. Yuan, Y. Cong, C. Fan, A. Westwood and X. Li, *Energy Storage Mater.*, 2020, **24**, 450–457.
97 W. Chai, F. Yang, W. Yin, S. You, K. Wang, W. Ye, Y. Rui and B. Tang, *Dalton Trans.*, 2019, **48**, 1906–1914.
98 T. Hou, B. Liu, X. Sun, A. Fan, Z. Xu, S. Cai, C. Zheng, G. Yu and A. Tricoli, *ACS Nano*, 2021, **15**, 6735–6746.
99 T. Li, L. Wang and J. Li, *Electrochim. Acta*, 2022, **408**, 139947.
100 L. Möller, E. Thauer, A. Ottmann, L. Deeg, R. Ghunaim, S. Hampel and R. Klingeler, *J. Alloys Compd.*, 2020, **834**, 155018.
101 K. P. Loh, Q. Bao, G. Eda and M. Chhowalla, *Nat. Chem.*, 2010, **2**, 1015–1024.
102 C. Lee, X. Wei, J. W. Kysar and J. Hone, *Science*, 2008, **321**, 385–388.
103 X. Wu, Z. Yang, L. Xu, J. Wang, L. Fan, F. Kong, Q. Shi, Y. Piao, G. Diao and M. Chen, *J. Energy Chem.*, 2022, **74**, 8–17.
104 A. Marrouche, B. Bouargane, A. Mabrouk, M. G. Biyoune, A. Bachar, A. Atbir, L. Boukbir, S. Mançour-Billah, R. Bellajrou and M. El Hadek, *Mediterr. J. Chem.*, 2019, **8**, 10–16.

Published on 11 July 2024. Downloaded on 4/29/2026 2:52:14 AM.